Available online at www.sciencedirect.com
ScienceDirect
Trans. Nonferrous Met. Soc. China 25(2015) 1158−1170
Transactions of Nonferrous Metals Society of China
www.tnmsc.cn

Correlation of microstructural and corrosion characteristics of quaternary shape memory alloys Cu−Al−Ni−X (X=Mn or Ti)

S. N. SAUD, E. HAMZAH, T. ABUBAKAR, H. R. BAKHSHESHI-RAD

Faculty of Mechanical Engineering, Universiti Teknologi Malaysia, Johor Bahru 81310, Johor, Malaysia

Received 18 April 2014; accepted 20 July 2014

Abstract: The effects of different contents (0.4%, 0.7%, and 1.0%, mass fraction) of Mn or Ti additions on the micro structure, shape memory effect and the corrosion behaviour of Cu−Al−Ni shape memory alloys were studied by field emission scanning electron microscopy, transmission electron microscopy, X-ray diffraction, differential scanning calorimetry and electrochemical and immersion tests in NaCl solution. It was observed that the microstructure, shape memory effect and corrosion characteristics are highly sensitive to the composition variations. It was found that the highest strain recovery was with 0.7% addition of Mn or Ti. This may be attributed to the presence of precipitation with a high volume fraction and the grain refinement. The electrochemical test showed that the formation of oxide layers in both Cu−Al−Ni−Mn and Cu−Al−Ni−Ti shape memory alloys (SMAs) provided good passivation which enhanced the corrosion resistance of the alloys. Immersion test showed that in Cu−Al−Ni−Mn SMAs, pitting corrosion occurred through feebleness in the oxide layer. A corrosion product adjacent to the pits was rich in Al/Mn oxide and depleted in Cu while inside of the pit it was rich in Cu. In Cu−Al−Ni−Ti SMAs, localized corrosion occurred on the surface of the specimens and dealuminization attack was also observed in the matrix.

Key words: Cu−Al−Ni alloy; shape memory effect; electrochemical test; alloying addition; microstructure

1 Introduction

Cu-based alloys are categorized in a group of functional, smart materials with the property of remembering the shape they had before the pseudoplastic deformation, known as shape memory alloys. Shape memory alloys are a group of metallic alloys with the remarkable potential to change from one crystallographic structure to another as a result of a change in temperature and/or applied stress. It is actually well-known that the shape memory properties are functions of microstructure, including grain size, texture and precipitation. These effects of Cu−Al−Ni alloys are dependent on crystallographic reversible thermoelastic martensitic transformation [1−3]. During the cooling process of the Cu−Al−Ni SMAs, the martensitic transformation exhibited from β-phase to a close packed structure. In the Cu−Al−Ni alloys, two types of thermal induced martensites (β'_1 and γ'_1) form depending on alloy composition and heat treatment [4−6]. However, the addition of alloying elements to Cu−Al−Ni alloys increases their mechanical properties and corrosion resistance while the presence of precipitates of Al/Ni−X (where X is the alloying element) is essential in the passivation of Cu−Al−Ni alloys. This is because of its incorporation in the Cu(I) oxide, which is formed on the corroded surface of the alloy. The corrosion behaviour of Cu−Al alloys in H_2SO_4 media was investigated by KUO et al [7], and their results showed that the addition of aluminium content slightly decreases pseudo-passive current density at the anodic potential. A formation of barrier film of Al_2O_3, which builds up quickly on the alloy surface, is the main reason for the enhancement of corrosion resistance of Cu−Al alloy [8]. However, other researchers attributed the enhancement of corrosion resistance to the formation of duplex layer composed of $Cu_2O{\cdot}Al_2O_3{\cdot}xH_2O$ as an inner layer which is covered with an outer layer [8]. The existence of Ni in binary Cu−Ni alloy leads to the improvement of corrosion resistance of the alloy due to the incorporation of Ni into the Cu_2O protective film through the solid-state reaction [9]. However, BADAWY et al [9] investigated the influence of nickel concentration on the corrosion behaviour of Cu−Al−Ni alloys in aqueous solutions and their result revealed that alloys with higher Ni content

Corresponding author: E. HAMZAH; E-mail: esah@mail.fkm.utm.my; safaaengineering@gmail.com
DOI: 10.1016/S1003-6326(15)63711-6

have a nickel-rich surface which decreases the corrosion resistance of the alloy. Several studies investigated the mechanical properties of Cu-shape memory alloys, while the electrochemical studies of Cu−Al−Ni−Mn and Cu−Al−Ni−Ti SMAs have not been reported elsewhere. The purpose of this work was to investigate the corrosion behaviour of Cu−Al−Ni−Mn and Cu−Al−Ni−Ti SMAs with different contents of Mn or Ti (0.4% to 1.0%) in a 3.5% NaCl solution. The effect of different contents of Mn or Ti addition on the microstructure and corrosion characteristics of Cu−Al−Ni alloys was also investigated.

2 Experimental

2.1 Preparation of materials

The chemical compositions of the Cu−Al−Ni SMA with and without the additions of Ti or Mn were investigated by inductively coupled plasma–mass spectrometry (ICP–MS). The specifications of the Cu−Al−Ni−X SMAs are shown in Table 1. The alloys were produced by melting metals in an induction furnace. These metals were melted in a silicon carbide crucible at a temperature of approximately 1300 °C for 25 min with continuous stirring and were then poured into a cast iron mould with dimensions of 270 mm×50 mm×20 mm. The ingot was homogenized at 900 °C for 30 min, and was then quenched in water, which led to the formation of martensite.

Flat specimens were cut from the cast ingot with dimensions of 10 mm×10 mm×2 mm for the microstructural observation and X-ray diffraction characteristics analysis. The phase identifications and crystal structure determinations were carried out with a D5000 Siemens X-ray diffractometer fitted with a Cu K_α X-ray source with a locked couple mode, 2θ range 30°−80°, and 0.05 (°)/s scanning step. Filings of the alloys removed were about 2−6 mg, and were taken for the DSC measurements (a Mettler Toledo DSC 822e) with a scanning rate of 10 K/min in the range of 323−573 K. The quenched samples were ground and polished and then etched into a solution containing 2.5 g ferric chloride acid ($FeCl_3·6H_2O$) and 48 mL methanol (CH_3OH) in 10 mL HCl for 4 min.

2.2 Shape memory test

The shape memory effect test was carried out with an Instron 5982-type universal testing machine, operated with special program parameters according to the shape memory test. The machine was connected with a heater tape and digital thermocouple to control the applied temperature, as well as an external extensometer to measure the shape extension and recovery. The tests were carried out at a temperature below M_f, which was about 100 °C, where the alloys would be able to obtain shape recovery. Then, the deformed sample that still had an unrecoverable shape was subsequently heated above the austenite finish temperature (A_f+ 60 °C) for 10 min, followed by water quenching to recover the residual strain (ε_r).

2.3 Electrochemical test

Rectangular specimens with a surface area of 1 cm^2 were moulded into epoxy resin for an electrochemical test. The test was conducted at 20°C in open air in a glass cell containing 350 mL of 3.5% NaCl solution by using a PARSTAT 2263 potentiostat/galvanostat (Princeton Applied Research). A three-electrode cell was used for potentiodynamic polarisation tests, where the reference electrode was a saturated calomel electrode (SCE). The counter electrode was made from a graphite rod and the specimen was the working electrode. All experiments were carried out at a constant scan rate of 0.5 mV/s, initiated at −250 mV (vs SCEbelow the open circuit potential. This fitting is inherently difficult; however, the software can allow for manual control. Tafel fittings were generally carried out by selecting a segment of the curve from φ_{corr}, and J_{corr} was subsequently estimated based on the value where the fit intercepted the potential value of the true φ_{corr} [10]. Each experiment was repeated twice to check the reproducibility of the results and all potentials were referred to SCE.

2.4 Immersion test

The immersion test was carried out according to the ASTM: G1–03. Twenty rectangular specimens with dimensions of 10 mm×15 mm×5 mm were cut and subsequently ground with 400–1000 grit SiC papers. The

Table 1 Chemical compositions and transformation temperatures of Cu−Al−Ni−X SMAs

Alloy No.	Mass fraction/%					A_s/K	A_f/K	M_s/K	M_f/K
	Cu	Al	Ni	Ti	Mn				
1	83.7	11.9	4	−	0.4	515.00	524.00	512.59	505.90
2	83.4	11.9	4	−	0.7	522.60	531.99	520.59	512.89
3	83.1	11.9	4	−	1.0	513.00	522.00	511.58	504.00
4	83.7	11.9	4	0.4	−	506.62	518.56	506.91	499.14
5	83.4	11.9	4	0.7	−	509.35	520.10	508.78	502.35
6	83.1	11.9	4	1.0	−	505.30	515.88	504.74	498.20

specimens were then washed thoroughly with distilled water, rinsed, ultrasonically degreased with ethanol, and subsequently dried at room temperature. The specimens were then immersed in a beaker containing 200 mL of 3.5% NaCl solution and were incubated at a constant temperature ((20±0.5) °C) for 10 d. The surface appearance of corroded specimens was assessed by SEM and EDS.

3 Results and discussion

3.1 Transformation temperatures and microstructural characteristics of Cu−Al−Ni−X SMAs

The transformation temperatures of Cu−Al−Ni−X SMAs (X=Ti or Mn) were determined and the data are given in Table 1. It was found that the transformation temperatures were varied according to the type and addition amount of the alloy element. The highest temperature was observed with the Mn addition of 0.7%. The transformation temperature changes occurred due to the variations of the martensite phase type and morphology. However, the type and amount of precipitates/intermetallic compounds may also have a remarkable influence on the transformation characteristics of Cu−Al−Ni−X SMAs.

In order to investigate the effect of Mn and Ti addition on the microstructural characteristics, field emission scanning electron microscope (FESEM) and transmission electron microscope (TEM) were used. Figure 1 shows the micrographs of Cu−Al−Ni SMAs with additions of Mn and Ti. It was found that all the microstructures obtained are in martensite state at room temperature with needle-like and plate-like morphologies. These morphologies are referred to as two types of

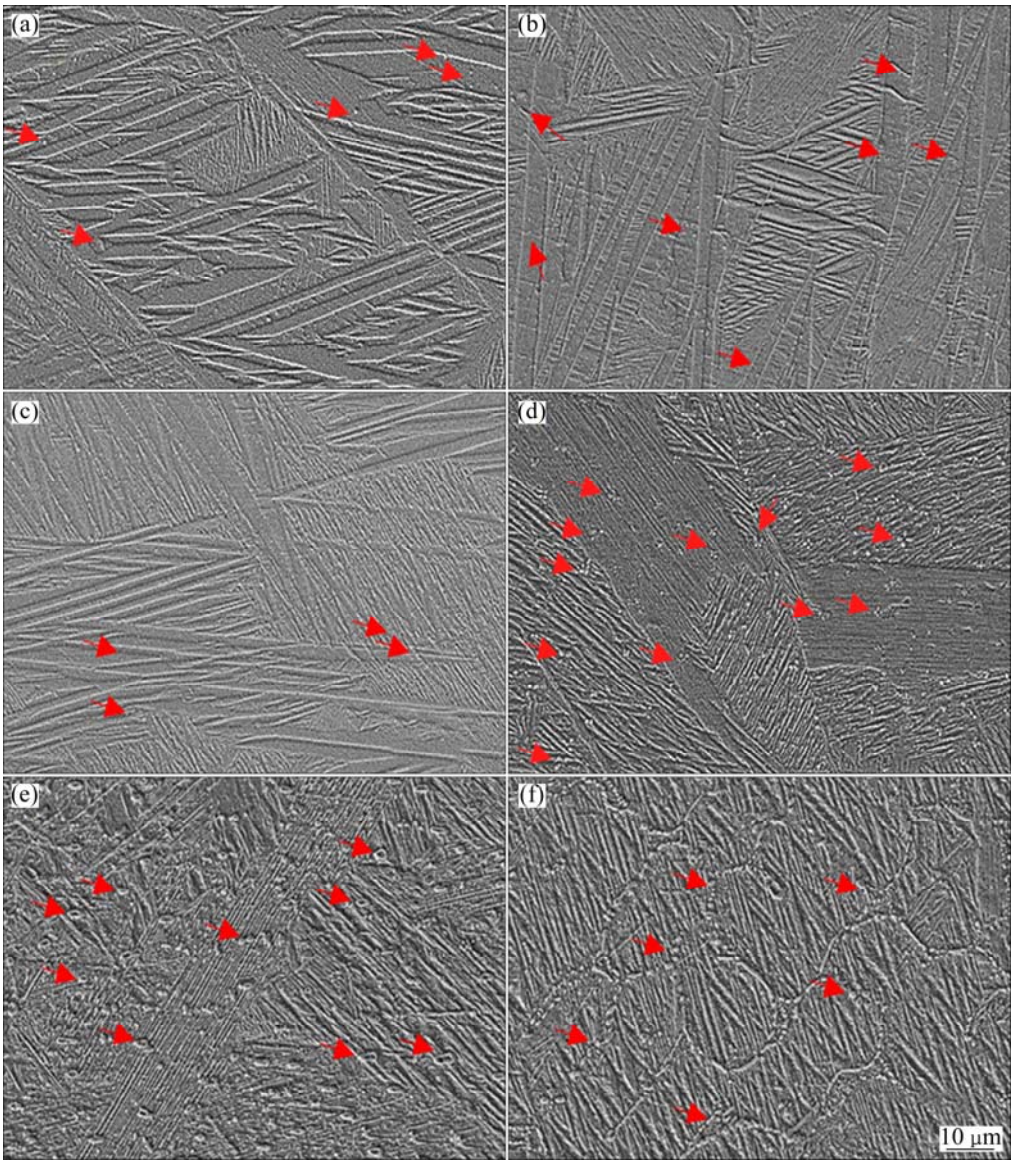

Fig. 1 Micrographs of Cu−Al−Ni−X alloys: (a) Cu−Al−Ni−0.4Mn; (b) Cu−Al−Ni−0.7Mn; (c) Cu−Al−Ni−1.0Mn; (d) Cu−Al−Ni−0.4Ti; (e) Cu−Al−Ni−0.7Ti; (f) Cu−Al−Ni−1.0Ti

thermal induced martensite: β'_1 and γ'_1 phases, where γ'_1 formed as a coarse plate-like phase, while β'_1 formed as a needle-like one between γ'_1 plate-like phases, associating with some precipitates are formed into the microstructure either between the parent phases or above them. The needle-like β'_1 martensite has very high thermo-elastic behaviour, which can be attributed to their controlled growth in the self-accommodating groups. However, the micrographs showed a self-accommodation plate-like martensite, whereas these plate-like martensites nucleated and grew up in different directions. The growth process of the martensite phase involves the accommodation of the local stress field, and therefore, it requires forming other groups [5].

According to the corresponding EDS (Figs. 2(a) and (b) and XRD patterns (Fig. 3), it is found that these precipitates/intermetallic compounds with the Mn addition are related to two phases: Al_8Mn_5 and Al_6Mn, while the addition of Ti forms a type of precipitates known as X-phase [11,12], which are related to the $Ni_3(Al,Ti)$, $Ni_{0.35}Al_{0.3}Ti_{0.35}$ and $Ti_{3.3}Al$ compounds. Recently, RATCHEV et al [13] mentioned that this phase has an equivalent composition and structure of the X phase, and it is also noticed that this phase has a strong influence on the stacking sequence of the plate-like martensite. With the Mn or Ti addition, the volume fraction of the precipitates reached the maximum with 0.7% addition, which is followed by the addition of 1%. The shape of precipitates with Mn addition is circular-like, and their size and distribution are varied with increasing addition amount of Mn from 0.4% to 1.0%, as shown in Figs. 1(a)−(c). Generally, with the Ti

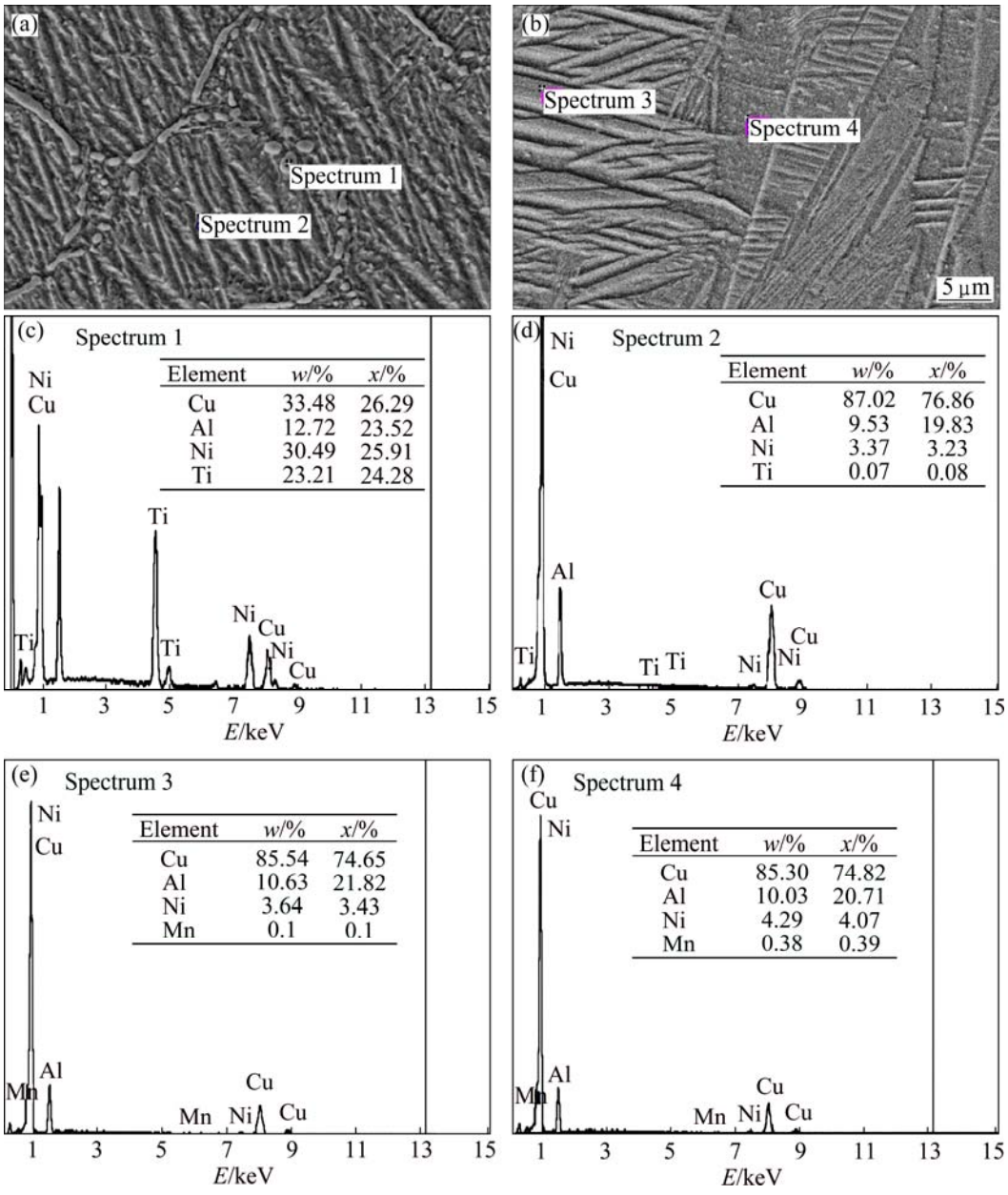

Fig. 2 EDS analysis of Cu−Al−Ni−1.0Ti (a, c, d) and Cu−Al−Ni−1.0Mn (b, e, f) SMAs

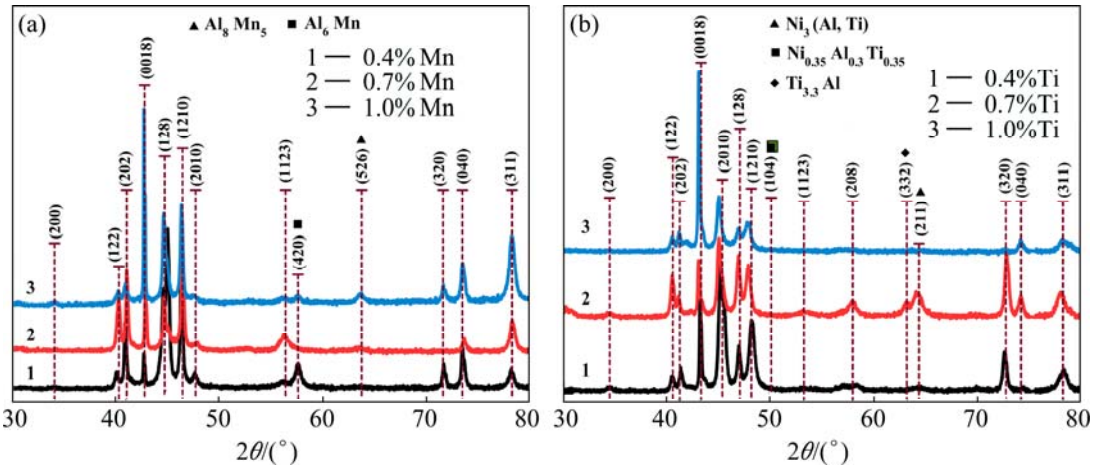

Fig. 3 XRD patterns of Cu−Al−Ni−Mn (a) and Cu−Al−Ni−Ti (b) SMAs

addition, the distribution of these precipitations is either between the plate-like and needle-like phases, or in an individual area [14], as shown in Figs. 1(d)−(f). This is the case for instance in which precipitates formed in a regular and irregular shape, and in which the regular shape looks like a flower-like shape. When the Ti addition is further increased to 1.0%, the X-phase starts to dissolve and creates visualized boundaries. Moreover, theses boundaries impede the growth of β'_1, as shown in Fig. 1(f). In the case of reduction of both precipitates' dispersion and grain sizes, the interface mobility can lead to a reduction in the martensite plate size [15]. Even though these precipitates are capable of restricting the growth of the plate-like martensite, they are also able to widen the transformation hysteresis [15,16]. From another point of view, the average grain size exhibits a significant difference between the alloys, whereas the grain size of the base alloy (Cu−Al−Ni) was around 1400 μm, as confirmed by other researchers [17,18]. It was also observed that with the addition of Mn, the grain size decreases to 600, 300, and 450 μm, respectively, while, it was observed that grains are refined to 900, 400, and 650 μm, with Ti addition. In other words, the grain size was decreased by about 80 % due to the Mn addition and grain size was reduced by about 70% after Ti was added. This attribution may show that Ti and Mn are able to diffuse very fast into the microstructure and accumulate at the grain boundaries, and then restrict grain growth. However, the grain refinement is also related to the inhibiting effect of grain growth of Ti and Mn in solid solution [18−20].

Figure 3 shows the XRD results of the Cu−Al−Ni SMA with Mn and Ti additions. It is found that the pattern peaks were shifted towards a higher angle with variation in their shape and intensity, which were caused by the Mn and Ti addition. However, the diffraction patterns of the alloys with additions have confirmed the existence of two metastable phases, γ'_1 and β'_1. The main diffraction patterns of the alloys are (122), (0018), (128), (1210), (2010), (208), (211), (040), (320), and (311), which indicate the presence of β'_1 martensite phase, while (200) and (202) indicate the presence of the γ'_1 martensite phase. However, with the Mn addition, two new peaks (420) and (526) are obtained, which represent the precipitate phases, i.e., Al_6Mn and Al_8Mn_5 compounds. On the other hand, the intensity of the corresponding peaks of precipitates is also varied according to the volume fraction of the precipitates, as highlighted in Fig. 3(a). With the Ti addition, three peaks are observed, (104), (332) and (211), at 2θ of 50.1°, 63.5° and 64.4°, i.e., Ni_3(Al, Ti), $Ni_{0.35}Al_{0.3}Ti_{0.35}$ and $Ti_{3.3}Al$ compounds, which in turn represented the X-phase, as shown in Fig. 3(b). By increasing Ti addition to 1%, these peaks disappeared progressively, with the exception of (211). This is attributed to a low density of X-phase in the microstructure which is due to the dissolving of these precipitates into the microstructure and creating grain boundaries, as confirmed by Fig. 1(f). Figure 4 shows the TEM images and selected area diffractions of the Cu−Al−Ni−0.7Mn and Cu−Al−Ni−0.7Ti SMAs. The analysis of the area diffraction patterns shows that the stacking sequence of the formed martensite is a monoclinic structure. It was observed that γ'_1 and β'_1 phases were obtained in correspondance with the existence of precipitates as indicated by the red dots. The stacking sequence of martensite also showed a monoclinic structure along with different positions of the peaks as indicated from Fig. 4. In addition, these peaks were distributed in an orbital zone around the [000].

3.2 Shape memory effect

The strain recovery by the shape memory effect (ε_{SME}) of the Cu−Al−Ni SMAs with Ti and Mn additions was determined by using a specially designed tensile test

at $T<M_f$. The ε_{SME} varied with the variation in the amount of Ti or Mn additions at the initial strain around 1.55 %, as shown in Fig. 5. It was indicated that the strain recovery by the shape memory effect (SME) increased from 66% to 100 % with the addition of Ti from 0.4% to 0.7%. However, when the amount of Mn increased from 0.4% to 0.7%, the alloys have recovered 90% of the original shape. It was observed that the additions of Ti or Mn exhibited an increase in the strain recovery by the SME. Both SMAs with 0.7% Ti or 0.7%Mn exhibited almost a complete shape recovery (100% of the original shape) after being preheated to $T>A_f$. These enhancements in the strain recovery were attributed to the existence of the precipitates and grain refinement, which was brought about by the addition of Ti or Mn in the parent phase.

3.3 Electrochemical measurements

Figure 6 displays the polarization curves for Cu−Al−Ni, Cu−Al−Ni−Mn and Cu−Al−Ni−Ti SMAs after 1 h exposure in 3.5% NaCl solution. Both experimental results of Cu−Al−Ni−0.4Mn and Cu−Al−Ni−0.4Ti SMAs showed less potential for the negative corrosion values of −286.5 mV and −289.4 mV, respectively compared with the base Cu−Al−Ni alloy (−307.4 mV). There was also a substantial difference in the corrosion current density of the Ti- and Mn-containing copper SMAs and Cu−Al−Ni alloy. Furthermore, addition of 0.7% Mn shifts the corrosion potential of base SMA to nobler direction by 40.1 mV and declines the current density from 6.93 μA/cm^2 to 1.43 μA/cm^2. The addition of 0.7% Ti to the base alloy also showed similar trends; it shifts the corrosion potential of base alloy to a more positive value (−249.1 mV) and decreases the current density (2.81 μA/cm^2). However, further addition of Mn or Ti to 1.0% negatively shifts the corrosion potential to –277.7 mV and −265.7 mV, respectively, and marginally increases the corrosion current density to 1.58 μA/cm^2 and 3.87 μA/cm^2, respectively. The addition of Mn and Ti for

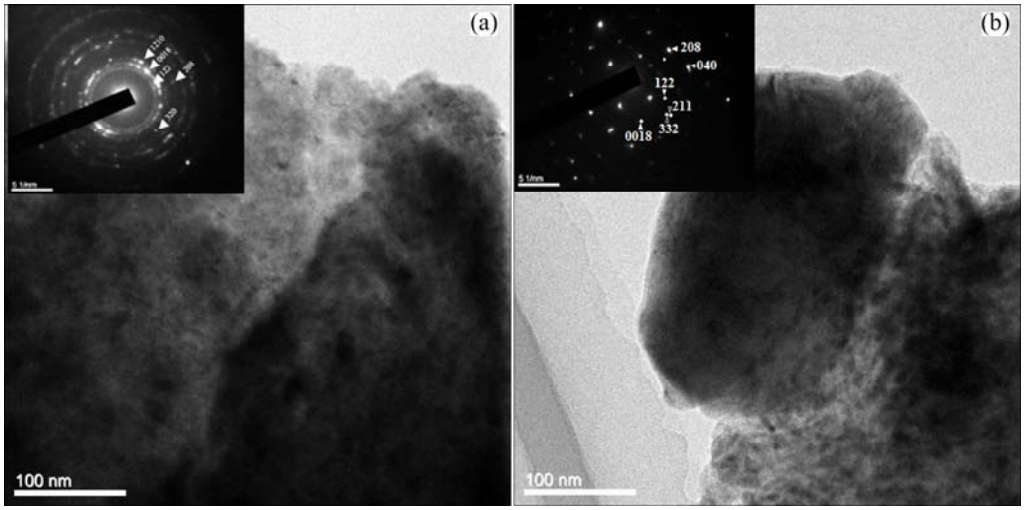

Fig. 4 TEM images and selected area diffraction of Cu−Al−Ni−0.7Mn (a) and Cu−Al−Ni−0.7Ti (b) SMA

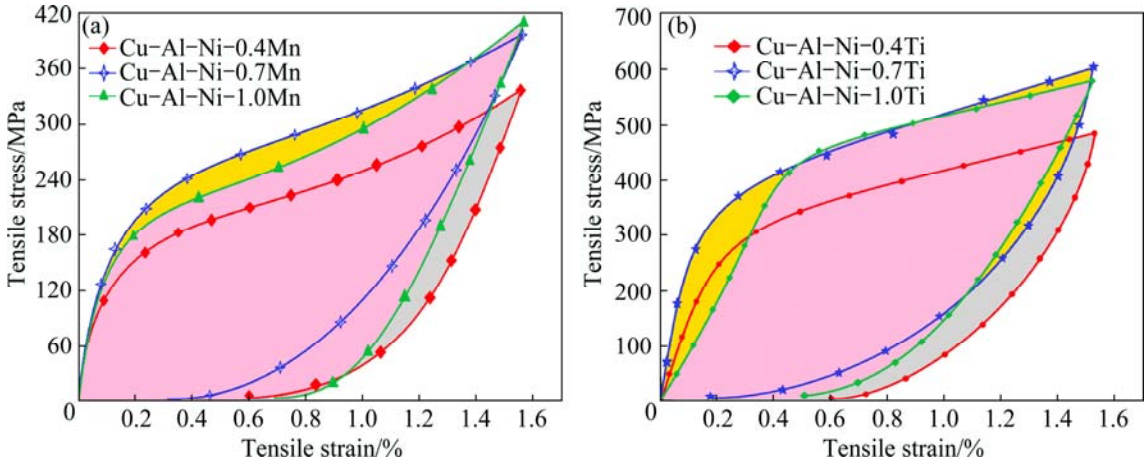

Fig. 5 Shape memory effect curves of Cu−Al−Ni−xMn (a) and Cu−Al−Ni−xTi SMAs (b) performed at $T<M_f$, then preheated to $T>A_f$

Cu−Al−Ni SMA decreases anodic polarization tendency while improving the cathodic polarization performance [21].

It can be suggested that decreasing the grain size as a result of Mn and Ti addition leads to the formation of passivation film, resulting in an increase of its resistance to pit nucleation. Moreover, the presence of Mn and Ti in the passivation film protects the SMAs from the aggressive action of Cl^- better than it does in the base alloy [22]. It was reported that grain refinement is an essential factor in determining the corrosion behaviour of the alloy. In this study, different addition amounts of Mn and Ti into the Cu−Al−Ni SMA lead to a reduction in grain size. This phenomenon leads to improvement in the compactness and stability of the passive film, resulting in significant improvement of the corrosion resistance of the SMAs [23]. In this regard, both Cu−Al−Ni−0.7Mn and Cu−Al−Ni−0.7Ti presented higher corrosion resistance compared with Cu−Al−Ni base alloy, which was due to the finer grain size of Cu−Al−Ni−Mn which resulted in the compactness and stability improvement of the passive film. The corrosion current density (J_{corr}), corrosion potential (φ_{corr}, vs SCE), cathodic Tefal slope (β_c), anodic Tefal slope (β_a) and corresponding corrosion rate (P_i) of specimens extracted from the polarization curves are shown in Table 2. The J_{corr} is related to the corrosion rate P_i through the following empirical equation [24−26].

$$P_i=22.85J_{corr} \quad (1)$$

The results also revealed that the corrosion rate of the specimens increased, in the order of Cu−Al−Ni−0.7Mn<Cu−Al−Ni−1Mn<Cu−Al−Ni−0.4Mn<Cu−Al−Ni SMAs. The corrosion rate of the Cu–Al–Ni SMA also decreased significantly from 158.8 to 64.20 μm/a after addition of 0.7% Ti. This can be attributed to the formation of the corrosion products on the electrode surface, which act as barrier films to protect the surface from aggressive solution, thus creating enhanced corrosion resistance. Other reason for lower corrosion current density of the Cu−Al−Ni−Mn than that of Cu−Al−Ni SMA is the formation of the products such as cuprous chloride (CuCl), and cuprous oxide (Cu_2O) as well as formation of aluminium oxide/hydroxide (Al_2O_3/$Al(OH)_3$), and Mn-containing copper alloys which contain a manganese oxide [27]. As the corrosion product forms on the specimen surface, the anodic reaction will be controlled by the mass transfer process due to the inhibition of diffusion rate of Cl^-, OH^-, Cu^+ and $CuCl^{-2}$ by the protective oxide film; while the

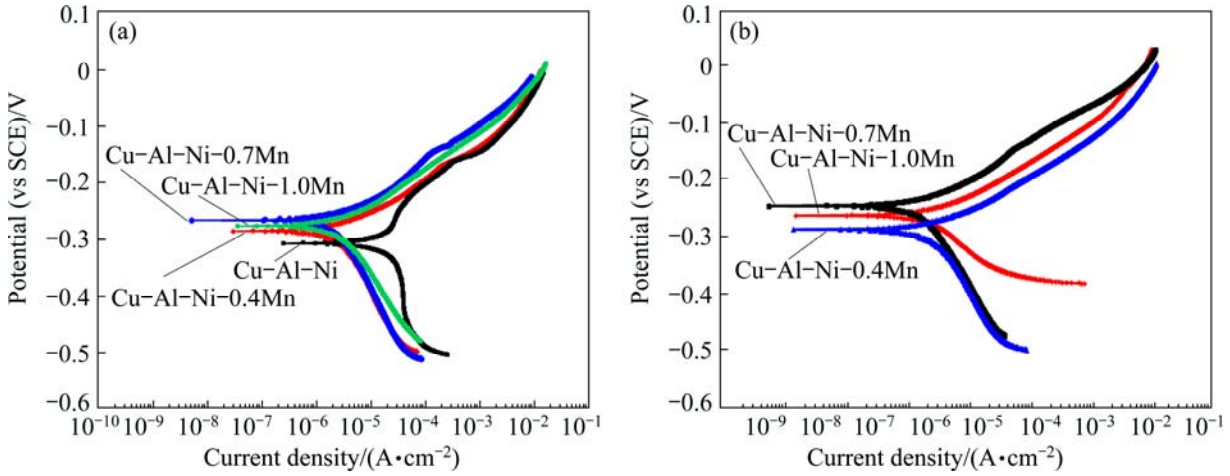

Fig. 6 Potentiodynamic polarization curves of Cu−Al−Ni−*x*Mn (a) and Cu−Al−Ni−*x*Ti (b) SMAs in 3.5% NaCl solution

Table 2 Electrochemical parameters of Cu−Al−Ni, Cu−Al−Ni−Mn and Cu−Al−Ni−Ti SMAs in NaCl solution by polarization test

Alloy	φ_{corr} (vs SCE)/mV	J_{corr}/ (μA·cm^{-2})	β_c (vs SCE)/ (mV·decade^{-1})	β_a(vs SCE)/ (mV·decade^{-1})	R_P/ (kΩ·cm^2)	P_i/ (μm·a^{-1})
Cu−Al−Ni	−307.4	6.93	198	88	3.82	158.18
Cu−Al−Ni−0.4Mn	−286.5	2.01	247	72	12.05	45.92
Cu−Al−Ni−0.7Mn	−267.3	1.43	256	79	16.61	32.67
Cu−Al−Ni−1.0Mn	−277.7	1.58	240	62	14.98	36.10
Cu−Al−Ni−0.4Ti	−289.4	4.33	192	54	4.23	98.94
Cu−Al−Ni−0.7Ti	−249.1	2.81	161	82	8.40	64.20
Cu−Al−Ni−1.0Ti	−265.7	3.87	116	58	4.34	88.42

diffusion of O_2 can proceed normally before the outer oxide film is formed.

The electrochemical parameters (J_{corr}, β_c and β_a) of specimens were also used to calculate the polarization resistance (R_P), according the following equation [24,28,29]:

$$R_P = \frac{\beta_a \beta_c}{2.3(\beta_a + \beta_c)J_{corr}} \quad (2)$$

The corrosion behavior of the alloy improved as R_P increased with the addition of Mn up to 0.7%. The addition of 0.7% Mn into the Cu−Al−Ni SMA significantly increased the R_P from 3.82 to 16.61 kΩ·cm^2. It was found that after addition of 0.7% Mn into Cu−Al−Ni SMA, the volume fraction of the precipitate increased, which resulted in decrease in the grain size of the Cu−Al−Ni SMA. This reduction of the grain size led to further increase in the polarization resistance of Cu−Al−Ni−0.7Mn compared with Cu−Al−Ni base alloy. The main reason of such improvement of corrosion resistance of the SMA with smaller grain size and higher volume fraction of the precipitate is the compactness and stability improvement of the passive film [30]. However, further addition of 1.0% Mn into Cu−Al−Ni alloy decreases R_P value to 14.98 kΩ·cm^2 due to the increase in grain size and less formation of precipitate. The additions of 0.4% and 0.7% Ti in the Cu−Al−Ni SMA also increased the R_p to 4.23 kΩ·cm^2 and 8.40 kΩ·cm^2, respectively, while further addition of Ti reversed the effect due to the aforementioned reason. The anodic Tafel slopes of both alloys were around 50−80 mV/decade, which is close to the theoretical and experimental value of 60 mV/decade [31]. This phenomenon indicated that the dissolution of copper into soluble $CuCl_2^-$ ion and soluble species from the electrode surface into bulk solution is a dominant corrosion mechanism for both alloys [27,32]. BENEDETI [32] reported that the corrosion behaviour of Cu−Al alloys is determined by aluminum dissolution accompanied with the copper dissolution. Formation of compact and protective film on the surface of Cu−Al−Ni−Mn alloy reduces the anodic dissolution rate.

3.4 Immersion test

Figure 7 shows the SEM micrographs of the Cu−Al−Ni−Mn SMAs after the immersion test in 3.5%

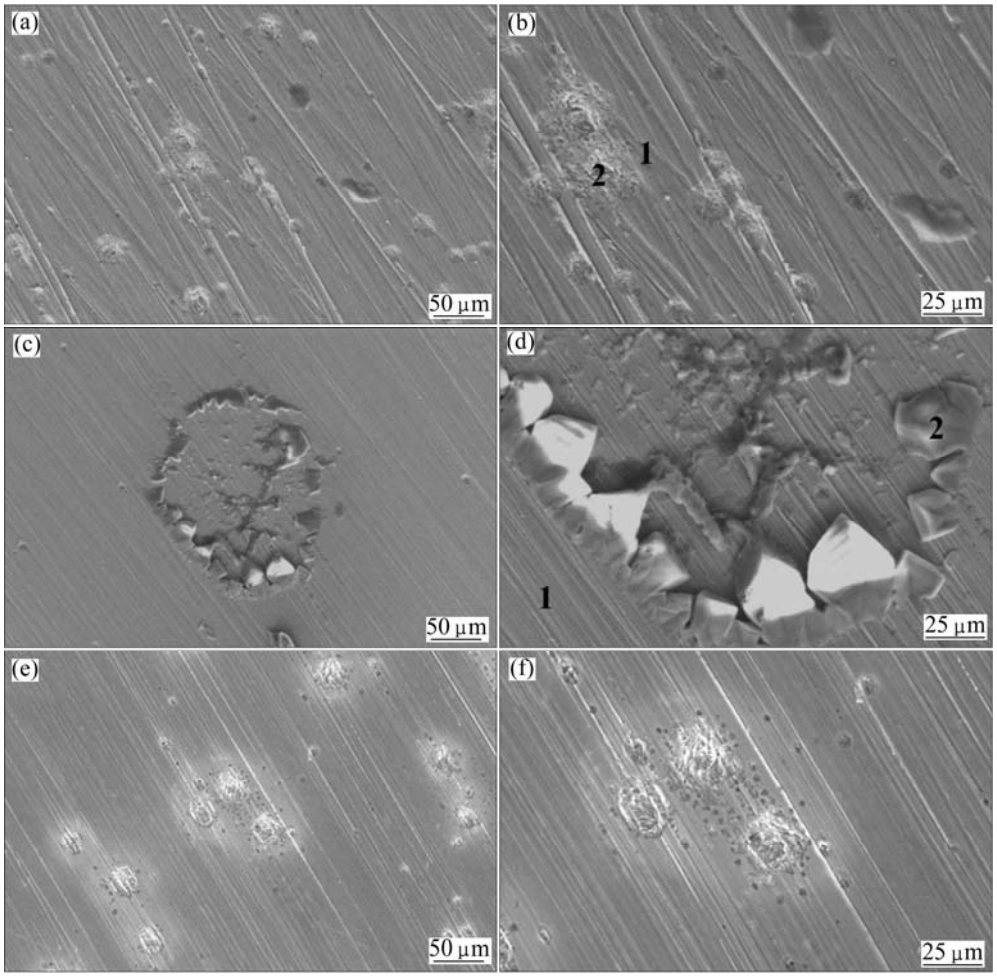

Fig. 7 SEM micrographs of Cu−Al−Ni−*x*Mn alloys in 3.5% NaCl with immersion duration of 240 h: (a,b) 0.4; (c,d) 0.7; (e,f) 1.0

NaCl solution. As 0.4% Mn was added to the Cu−Al−Ni SMA, some pits were produced by dealuminizations, which were detected in the matrix. Pitting corrosion was explained by local galvanic reactions. Since Cu is nobler than Mn, Al and Ni, there was a selective dissolution of Mn, Al and Ni in Cu-based alloy in NaCl [33]. EDX analysis showed that the pit was depleted in Mn, Al and Ni and enriched in Cu (area 2), while the area adjacent to the pits is enriched in Mn, Al, Ni and O (area 1), as seen in Table 3. Aggressive Cl^- ions can induce pitting and models generally propose adsorption of the chloride, diffusion of the chloride through the surface film via dislocations, cracks, grain boundaries or point defects and increase the corrosion rate of the alloy. With further addition of 0.7% Mn, the matrix was slightly impoverished in Al and a large amount of corrosion products formed on the surface of the alloy (area 1). EDX analysis further confirmed that the precipitates present a surface film rich in O, Al, Cu, Ni and Mn, which would correspond to Al_2O_3, Cu_2O, $Al(OH)_3$ and Mn_2O_3, and a small amount of Cl which would attributed to the $Cu_2Cl(OH)_3$, $Mn(ClO_4)$ (area 2) as seen in Table 3. It was reported that the formation of an oxide layer has a negligible effect on the cathodic process, but reduces the anodic dissolution rate [9]. The amount of pits increased with the addition of 1.0% Mn. This pit was produced by severe dealuminization which was observed in the matrix. Pitting was accompanied by removal of the surface Mn/Al-rich oxides and accumulation of products around the pit. These losses can be qualitatively explained by localized galvanic reactions in the alloy [33,34]. It was reported that chlorides spread radially along the alloy/oxide interface and it has deleterious effect on the overlaying oxides [33]. The standard electrode potentials (vs SCE) of Cu, Mn, Al and Ni are −0.16 V (Cu/Cu^{2+}), −1.18 V (Mn/Mn^{2+}), −1.66 V (Al/Al^{3+}) and −0.23 V (Ni/Ni^{2+}), respectively. As such, Cu is the most noble of the metals and Al is the least noble and so the range of potentials is in the following order: Cu>Ni>Mn>Al. Therefore, Al, Mn and Ni would be more likely to electrochemically be oxidized before the Cu component and resulted in formation of the pits with deficient elements [33]. EDX analysis also showed that the surface of 0.4% Mn-containing alloys is richer in Cl than that of the 0.7% Mn alloy. In addition, the surface of the Cu−Al−Ni−0.7Mn is rich in Cu, Al, Ni and Mn and the Cl is less, resulting in surface passivation and lower corrosion rate of the alloy [31]. It exhibited that the chloride ions easily penetrated the alloy surface due to its small radius and led to an increase in pH of the solution and consequently promoted further dissolution of the substrate [35].

SEM images of Cu−Al−Ni−Ti SMAs show the occurrence of localized corrosion on the surface of the specimens (Fig. 8). Cu−Al−Ni−0.4T SMA presents some areas with severe localized corrosion. The EDX analysis of different areas was given in Table 4. According to the EDX analysis, area 1 is composed of a large amount of Cu, O and Al and a few Cl, Ni and Ti. This indicated that the matrix was impoverished in Al and formation of CuO, Cu_2O, and $CuCl_2$ in the matrix [34]. It was reported that $CuCl_2$ salt layer formed on Cu−Al alloys may be incorporated with the Al salt films such as AlCl and $Al(OH)_2Cl$ [34]. However, area 2 is composed of NaCl and corrosion products such as CuO, Cu_2O, and Al_2O_3. Area 3 was produced by a severe dealuminization which can clearly be observed in the matrix (Figs. 8(a) and (b)). In Cu−Al−Ni−0.7Ti SMA, three different morphological zones can be observed. Area 1 indicated particles which are rich in O and Al, indicating the formation of Al_2O_3 while it is depleted in Cu. However, corrosion product was absent in area 3, which shows that the surface was mostly uncorroded (Figs. 8(c) and (d)). In contrast, the precipitates (area 2) were enriched in Ti and Al in comparison to area 3, indicating the formation of mixed Al/Ti oxide corrosion product which would correspond to Al_2O_3, TiO_2 and Al_2TiO_5. However, after the addition of 1% Ti into the Cu−Al−Ni SMA, the amount of precipitates with round and cubic morphology significantly increased; these precipitates were completely dark or bright with respect to the matrix color (Figs. 8(e) and (f)). In this regard, the high corrosion resistance of Ti-containing copper alloys is attributed to the spontaneous formation of a compact and adherent oxide layer that is rapidly regenerated if damaged in air. It was reported that in aqueous media, the growth of the oxide film through metal oxidation simultaneously competes with its slow dissolution [33]. Some of the dissolved TiO_2 precipitates as an outer hydroxide layer and enhances the corrosion resistance of the alloy. When Cu-based alloy specimens were exposed to the NaCl solution, Cu elements dissolved and a corrosion layer was deposited according to the following reactions [31]:

Table 3 EDX analysis of Cu−Al−Ni−*x*Mn SMAs after immersion test in 3.5% NaCl (Areas 1 and 2 correspond with EDS point analyses shown in Fig. 7)

Alloy	Area	Mass fraction/%						
		Cu	Al	Ni	O	Cl	C	Mn
Cu−Al−Ni−0.4Mn	Area 1	44.21	9.91	4.54	29.21	8.51	3.28	0.34
	Area 2	84.12	2.54	0.32	9.74	0.43	2.85	–
Cu−Al−Ni−0.7Mn	Area 1	53.20	17.11	4.25	16.57	3.47	5.40	–
	Area 2	24.51	27.23	8.54	29.92	4.32	4.73	0.75

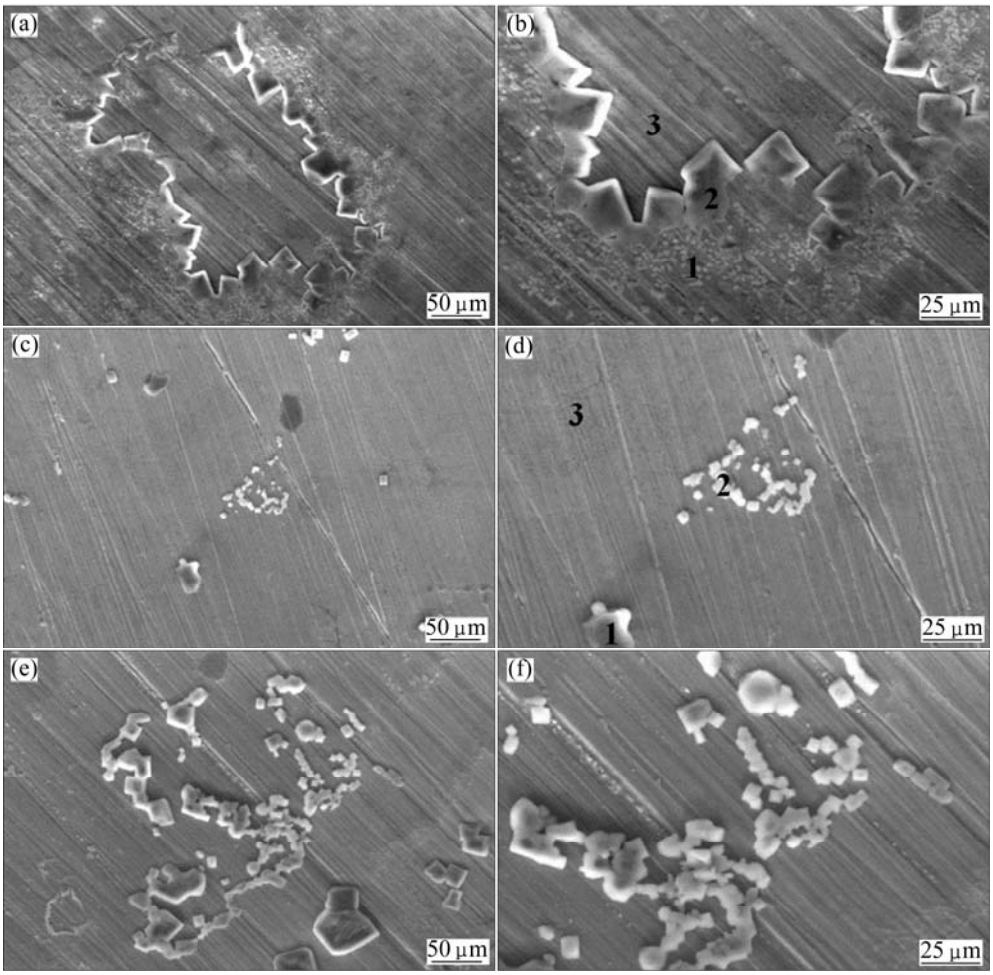

Fig. 8 SEM micrographs of Cu−Al−Ni−*x*Ti alloys with various Ti contents in 3.5% NaCl with immersion duration of 240 h: (a,b) 0.4; (c,d) 0.7; (e,f) 1.0

Table 4 EDX analysis of Cu−Al−Ni−*x*Ti SMAs after immersion test in 3.5% NaCl (Areas 1−3 correspond with EDS point analyses shown in Fig. 8)

Alloy	Area	Mass fraction/%						
		Cu	Al	Ni	O	Cl	C	Ti
Cu−Al−Ni−0.4Ti	Area 1	35.40	22.74	4.78	24.97	7.34	5.46	0.21
	Area 2	48.25	17.14	2.17	14.47	14.23	3.74	–
	Area 3	79.10	2.42	0.75	13.28	1.56	2.89	–
Cu−Al−Ni−0.7Ti	Area 1	21.72	30.45	3.78	40.76	2.12	1.17	–
	Area 2	76.21	7.73	1.46	9.11	0.83	4.35	–
	Area 3	42.41	27.34	7.18	13.97	0.65	8.44	0.32

$$O_2+2H_2O+4e\rightarrow 4OH^- \quad (3)$$

$$Cu+2Cl^-\rightarrow CuCl_2^-+e \quad (4)$$

The cathodic reaction occurred accompanied with the reduction of oxygen while the anodic reaction is the copper dissolution to form a dichlorocuprous anion complex [36]. The existence of $CuCl^{2-}$ on the surface of Cu based alloy resulted in a hydrolysis reaction and the formation of cuprous oxide (Cu_2O) according to the following reaction:

$$2CuCl_2^-+H_2O\rightarrow Cu_2O+4Cl^-+2H^+ \quad (5)$$

It was reported that the stable corrosion products formed on all the phases after long periods of immersion are $CuCl_2$ and a Cu_2O/CuO double layer surface film [36].

In Cu−Al−Ni SMA, a passivation process occurred in neutral solutions in which a Al-oxide layer is formed due to the surface dissolution of Al according to the following reactions:

$$Al+4Cl^-\rightarrow AlCl_4^-+3e \quad (6)$$

$$AlCl_4^- + 3H_2O\rightarrow Al_2O_3+6H^++8Cl^- \quad (7)$$

The dissolution Al_2O_3 increased in the NaCl solutions and corrosion product is formed according to the following reactions [21]:

$$Al^{3+}(\text{in } Al_2O_3.nH_2O \text{ crystal lattice})+Cl^-\rightarrow Al(OH)_2Cl+2H^+ \quad (8)$$

or

Al^{3+}(in $Al_2O_3.nH_2O$ crystal lattice)+$2Cl^-$→
$Al(OH)_2Cl_2^-+2H^+$ (9)

The progression of these reactions leads to thinning of the barrier film or even breakdown in some places. The hydrolysis process causes local acidity and accelerated dealuminumification corrosion continues [21,31].

The Mn oxy/hydroxides in the Cu−Al−Ni−Mn SMA also formed according the following equations [37]:

$Mn^{2+}+2H_2O→Mn(OH)_2+2H^+$ (10)

$2Mn(OH)_2+O_2→2MnO_2+2H_2O$ (11)

This formation can be attributed to an increase in the local pH level at the interface, which is caused by strong hydrogen evolution. This initially leads to metal hydrolysis and subsequently to further oxidation of metal hydroxides [37].

In the Cu−Al−Ni−Ti SMA, TiO_2 as an outer layer formed according to the following equations [33]:

$Ti^{3+}+2H_2O→TiO_2+4H^++e$ (12)

$TiO_2+4H^++Cl^-+e→TiCl^{2+}+2H_2O$ (13)

Figure 9 shows the XRD patterns of the Cu−Al−Ni−Mn specimens after 14 d of immersion in NaCl solution. The XRD analysis further confirmed the existence of $Al(OH)_2$, Mn_2O_3, $Cu_2Cl(OH)_3$, $CuMnO_2$, $Mn(ClO_4)$ on the surface of the sample beside Cu reflections. The strong diffraction intensities of $CuMnO_2$ and Mn_2O_3 phases in Cu−Al−Ni−0.7Mn SMA also indicate the formation of a compact and adherent Mn-oxide layer on the specimen surface (Fig. 9(a)). However, Cu−Al−Ni−Ti specimens show the presence of Al_2O_3, Al_2TiO_5, $Cu(ClO_4)_2$, TiO_2, $CuAl_2O_4$, $CuAlCl_4$, $TiCl_2$ phases reflections accompanied with Cu as shown in Fig. 9(b). As can be seen, the highest reflections of TiO_2 and Al_2TiO_5 can be identified in the Cu−Al−Ni−0.7Ti SMA, indicating the formation of Ti-oxide barrier film on the substrate surface, which can improve corrosion resistance of Ti-containing copper alloys.

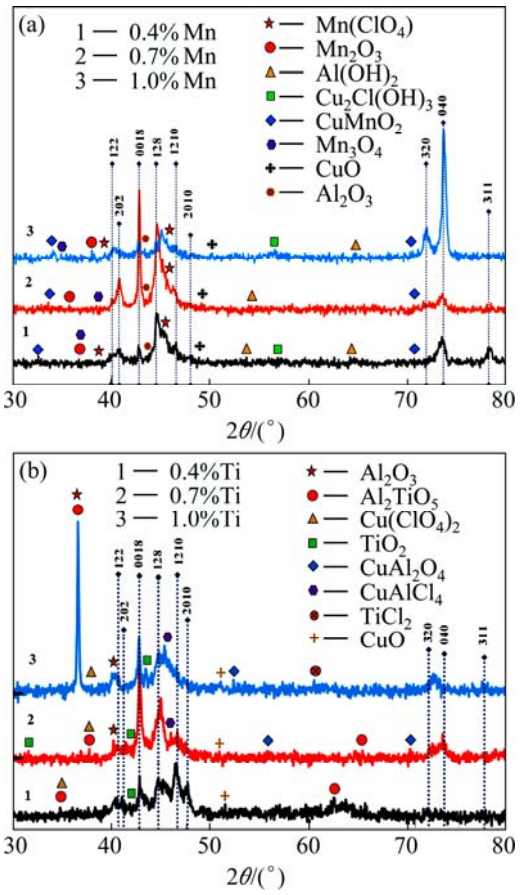

Fig. 9 XRD patterns of Cu−Al−Ni−*x*Mn (a) and Cu−Al−Ni−*x*Ti (b) SMAs after full immersion exposure in 3.5% NaCl for 240 h

4 Conclusions

The results show that with the increase in the amount of Mn or Ti addition, the grain size decreases initially and then increases. With the increase in the Mn or Ti content, the plate- and needle-like martensites coarsen and the volume fraction is also increased, and the highest size and volume fraction were obtained with 0.7% Mn or 0.7% Ti. It was also found that the martensite and austenite transformation temperatures were varied according to the type and amount of alloy addition. However, the highest temperature was observed with the addition of 0.7% Mn. Electrochemical tests showed that the corrosion potentials of both Cu−Al−Ni−Mn and Cu−Al−Ni−Ti SMAs shifted towards a nobler direction with 0.7% Mn or 0.7% Ti. This can be attributed to the formation of small grain size and high volume fraction of the precipitate which resulted in compactness and stability improvement of the passive film. However, further addition of 1.0% Mn or 1.0% Ti into quaternary alloy has the reverse effect. Immersion tests showed that pitting corrosion occurred through local galvanic reactions in Cu−Al−Ni−Mn. Since Cu is nobler than Al, Ni and Mn, the inside of the pit is rich in Cu whilst it is depleted in Al, Ni and Mn. Corrosion products composed of Al/Mn oxide accumulated adjacent to the pit. In Cu−Al−Ni−Ti SMAs, localized corrosion occurred on the surface of the specimens and dealuminization attack was also observed in the matrix. Both quaternary Cu−Al−Ni−Mn and Cu−Al−Ni−Ti SMAs presented higher corrosion resistance compared with ternary Cu−Al−Ni SMA.

Acknowledgements

The author(s) would like to thank the Malaysian Ministry of Higher Education (MOHE) and Universiti

Teknologi Malaysia for providing the financial support and facilities for this research, under Grant No. R.J130000.7824.4F150.

References

[1] FONT J, CESARI E, MUNTASELL J, PONS J. Thermomechanical cycling in Cu−Al−Ni-based melt-spun shape-memory ribbons [J]. Materials Science and Engineering A, 2003, 354: 207−211.

[2] TATAR C, ZENGIN R. The effects of γ-irradiation on some physical properties of Cu−13.5%Al−4%Ni shape memory alloy [J]. Materials Letters, 2005, 59: 3304−3307.

[3] OTSUKA K, REN X. Recent developments in the research of shape memory alloys [J]. Intermetallics, 1999, 7: 511−528.

[4] DAGDELEN T G F, AYDOGDU A, AYDOGDU Y, ADIGU ZEL O. Effects of thermal treatments on transformation behaviour in shape memory Cu−Al−Ni alloys [J]. Materials Letters, 2003, 57: 1079−1085.

[5] SARI U. Influences of 2.5wt% Mn addition on the microstructure and mechanical properties of Cu−Al−Ni shape memory alloys [J]. Int J Miner Metall Mater, 2010, 17: 192−198.

[6] SARI U, AKSOY İ. Electron microscopy study of 2H and 18R martensites in Cu−11.92wt% Al−3.78wt% Ni shape memory alloy [J]. Journal of Alloys and Compounds, 2006, 417: 138−142.

[7] KUO H, WANG W, HSU Y, HUANG C. The corrosion behavior of Cu−Al and Cu−Al−Be shape-memory alloys in 0.5 M H_2SO_4 solution [J]. Corrosion Science, 2006, 48: 4352−4364.

[8] BADAWY W, EL-RABIEI M, NADY H. Synergistic effects of alloying elements in Cu-ternary alloys in chloride solutions [J]. Electrochimica Acta, 2014, 120: 39−45.

[9] BADAWY W, EL-RABIEE M, HELAL N, NADY H. Effect of nickel content on the electrochemical behavior of Cu−Al−Ni alloys in chloride free neutral solutions [J]. Electrochimica Acta, 2010, 56: 913−918.

[10] SUDHOLZ A, GUSIEVA K, CHEN X, MUDDLE B, GIBSON M, BIRBILIS N. Electrochemical behaviour and corrosion of Mg−Y alloys [J]. Corrosion Science, 2011, 53: 2277−2282.

[11] HURTADO P R I, van HUMBEECK J, DELAEY L. A fundamental study of the X-phase preciptation in Cu−Al−Ni−Ti−(Mn) shape memory alloys [J]. Acta Materialia, 1995, 44: 3299−3306.

[12] WAYMAN J S L C M. Grain refinement of a Cu−Al−Ni shape memory alloy by Ti and Zr additions [J]. Transactions of the Japan Institute of Metals, 1986, 27: 584−591.

[13] RATCHEV P, van HUMBEECK J, DELAEY L. On the formation of 2H stacking sequence in 18R martensite plates in a precipitate containing CuAlNiTiMn alloy [J]. Acta Metallurgica Et Materialia, 1993, 41(8): 2441−2449.

[14] SUGIMOTO K, KAMEI K, MATSUMOTO H, KOMATSU S, AKAMATSU K, SUGIMOTO T. Grain-refinement and the related phenomena in quaternary Cu−Al−Ni−Ti shape memory alloys [J]. Le Journal de Physique Colloques, 1982, 43: C4-761−C764-766.

[15] MALARRÍA J, ELGOYHEN C, VERMAUT P, OCHIN P, PORTIER R. Shape memory properties of Cu-based thin tapes obtained by rapid solidification methods [J]. Materials Science and Engineering A, 2006, 438−440: 763−767.

[16] DUTKIEWICZ J, PONS J, CESARI E. Effect of γ precipitates on the martensitic transformation in Cu−Al−Mn alloys [J]. Materials Science and Engineering A, 1992, 158: 119−128.

[17] FUNAKUBO H. Shape memory alloys [M]. New York: Taylor & Francis, 1987.

[18] SAMPATH V. Studies on the effect of grain refinement and thermal processing on shape memory characteristics of Cu−Al−Ni alloys [J]. Smart Materials and Structures, 2005, 14: S253−S260.

[19] SURE G N, BROWN L C. The mechanical properties of grain refined β- cuaini strain-memory alloys [J]. Metallurgical Transactions A, 1984, 15: 1613−1621.

[20] LEE J, WAYMAN C. Grain refinement of a Cu−Al−Ni shape memory alloy by Ti and Zr additions [J]. Trans Jpn Inst Met, 1986, 27: 584−591.

[21] CHEN B, LIANG C, FU D, REN D. Corrosion behavior of Cu and the Cu−Zn−Al shape memory alloy in simulated uterine fluid [J]. Contraception, 2005, 72: 221−224.

[22] PISAREK M, KĘDZIERZAWSKI P, PŁOCIŃSKI T, JANIK-CZACHOR M, KURZYDŁOWSKI K J. Characterization of the effects of hydrostatic extrusion on grain size, surface composition and the corrosion resistance of austenitic stainless steels [J]. Materials Characterization, 2008, 59: 1292−1300.

[23] BALUSAMY S K T, SANKARA NARAYANAN T S N. Effect of surface nanocrystallization on the corrosion behavior of AISI 409 stainless steel [J]. Corrosion Science, 2010, 52: 3826−3834.

[24] BAKHSHESHI-RAD H, IDRIS M, ABDUL-KADIR M. Synthesis and in vitro degradation evaluation of the nano-HA/MgF_2 and DCPD/MgF_2 composite coating on biodegradable Mg–Ca–Zn alloy [J]. Surface and Coatings Technology, 2013, 222: 79−89.

[25] KASSAB E N, FROTSCHER L, SWAMINATHAN M, MAAß S, ROHWERDER B, GOMES M, EGGELER J G. Effect of ternary element addition on the corrosion behaviour of NiTi shape memory alloys [J]. Materials and Corrosion, 2014, 65: 18−22.

[26] MALEKI-GHALEH H K A, KHALILI J, SHAKERI V, JAVIDI M S M. Effect of hydroxyapatite coating fabricated by electrophoretic deposition method on corrosion behavior and nickel release of NiTi shape memory alloy [J]. Material and Corrosion, 2013, 65(7): 725−732.

[27] GOJIĆ M, VRSALOVIĆ L, KOŽUH S, KNEISSL A, ANŽEL I, GUDIĆ S, KOSEC B, KLIŠKIĆ M. Electrochemical and microstructural study of Cu–Al–Ni shape memory alloy [J]. Journal of Alloys and Compounds, 2011, 509: 9782−9790.

[28] BAKHSHESHI-RAD E H H R, MEDRAJ M, FEREIDOUNI-LOTFABADI A, DAROONPARVAR M, YAJID M A M, MEZBAHUL-ISLAM M, KASIRI-ASGARANI M. Microstructure and bio-corrosion behavior of Mg–Zn and Mg–Zn–Ca alloys for biomedical applications [J]. Materials and Corrosion, 2014, 65(12): 1178−1187.

[29] BAKHSHESHI-RAD E H H R, MEDRAJ M, IDRIS M H, DAROONPARVAR M, LOTFABADI A F, YAJID M A M. Effect of heat treatment on the microstructure and corrosion behaviour of Mg–Zn alloy [J]. Materials and Corrosion, 2013, 65(10): 999−1006.

[30] BALUSAMY T, KUMAR S, SANKARA NARAYANAN T S N. Effect of surface nanocrystallization on the corrosion behaviour of AISI 409 stainless steel [J]. Corrosion Science, 2010, 52: 3826−3834.

[31] MONTECINOS S, SIMISON S N. Influence of the microstructure on the corrosion behaviour of a shape memory Cu–Al–Be alloy in a marine environment [J]. Applied Surface Science, 2011, 257: 2737−2744.

[32] BENEDETI A, SUMODJO P, NOBE K, CABOT P, PROUD W. Electrochemical studies of copper, copper-aluminium and copper−aluminium−silver alloys: Impedance results in 0.5 M NaCl [J]. Electrochimica Acta, 1995, 40: 2657−2668.

[33] BACA N, CONNER R, GARRETT S. Corrosion behavior of oxide-covered $Cu_{47}Ti_{34}Zr_{11}Ni_8$(Vitreloy 101) in chloride-containing solutions [J]. Materials Science and Engineering B, 2014, 184: 105−112.

[34] MONTECINOS S, SIMISON S. Corrosion behavior of Cu−Al−Be shape memory alloys with different compositions and microstructures [J]. Corrosion Science, 2013, 74: 387−395.

[35] BAKHSHESHI-RAD H, ABDUL-KADIR M, IDRIS M,

FARAHANY S. Relationship between the corrosion behavior and the thermal characteristics and microstructure of Mg–0.5Ca_xZn alloys [J]. Corrosion Science, 2012, 64: 184−197.

[36] MONTECINOS S, SIMISON S. Study of the corrosion products formed on a multiphase CuAlBe alloy in a sodium chloride solution by micro-Raman and in situ AFM measurements [J]. Applied Surface Science, 2011, 257: 7732−7738.

[37] HAERIFAR M, ZANDRAHIMI M. Effect of current density and electrolyte pH on microstructure of Mn–Cu electroplated coatings [J]. Applied Surface Science, 2013, 284: 126−132.

四元形状记忆合金 Cu−Al−Ni−X (X=Mn,Ti)的显微组织和腐蚀特征

S. N. SAUD, E. HAMZAH, T. ABUBAKAR, H. R. BAKHSHESHI-RAD

Faculty of Mechanical Engineering, Universiti Teknologi Malaysia, Johor Bahru 81310, Johor, Malaysia

摘　要：采用场发射扫描电子显微镜、透射电子显微镜、X 射线衍射和差示扫描量热法，并在 NaCl 溶液中进行电化学和浸渍试验，研究添加不同含量的 Mn 或 Ti(0.4%，0.7%，和 1.0%，质量分数)对 Cu−Al−Ni 形状记忆合金的显微组织、形状记忆效应和腐蚀行为的影响。研究结果表明，显微组织、形状记忆效应和腐蚀特征对成分变化高度敏感。当添加 0.7% Mn 或 0.7% Ti 时，合金出现了最高的应变回复率。这可能是由于存在晶粒细化和高体积分数沉淀。电化学测试表明，在 Cu−Al−Ni−Mn 和 Cu−Al−Ni−Ti 形状记忆合金中氧化层的形成提供了良好的钝化保护，从而提高了合金的耐蚀性。浸渍试验表明，在 Cu−Al−Ni−Mn 形状记忆合金中，氧化层发生了点状腐蚀。腐蚀坑附近的腐蚀产物富 Al/Mn 氧化物而贫铜，而在腐蚀坑内腐蚀产物富铜。在 Cu− Al− Ni− Ti 形状记忆合金样品表面发生了局部腐蚀，而在基体中发生了脱铝腐蚀。

关键词：Cu−Al−Ni 合金；形状记忆效应；电化学测试；添加合金；微观组织

(Edited by Xiang-qun LI)